



HAL
open science

Ultra wide band frequency characterization of integrated TiTaO-based metal-insulator-metal devices

Thomas Bertaud, Cedric Bermond, Fatiha Challali, Antoine Goullet,
Christophe Vallee, Bernard Flechet

► To cite this version:

Thomas Bertaud, Cedric Bermond, Fatiha Challali, Antoine Goullet, Christophe Vallee, et al.. Ultra wide band frequency characterization of integrated TiTaO-based metal-insulator-metal devices. Journal of Applied Physics, 2011, 110 (4), pp.044110. 10.1063/1.3626067 . hal-00849729

HAL Id: hal-00849729

<https://hal.science/hal-00849729>

Submitted on 9 May 2022

HAL is a multi-disciplinary open access archive for the deposit and dissemination of scientific research documents, whether they are published or not. The documents may come from teaching and research institutions in France or abroad, or from public or private research centers.

L'archive ouverte pluridisciplinaire **HAL**, est destinée au dépôt et à la diffusion de documents scientifiques de niveau recherche, publiés ou non, émanant des établissements d'enseignement et de recherche français ou étrangers, des laboratoires publics ou privés.

Ultra wide band frequency characterization of integrated TiTaO-based metal–insulator–metal devices

Thomas Bertaud,^{1,2,4,a)} Cédric Bermond,¹ Fatiha Challali,³ Antoine Goullet,³ Christophe Vallée,² and Bernard Fléchet¹

¹Université de Savoie, IMEP-LAHC, UMR CNRS 5130, 73376 Le Bourget du Lac, France

²Université de Grenoble, LTM, UMR CNRS 5129, 38054 Grenoble Cedex 9, France

³Université de Nantes, IMN, UMR 6205, B.P.32229, 44322 Nantes cedex 3, France

⁴IHP, Im Technologiepark 25, 15236 Frankfurt (Oder), Germany

(Received 20 April 2011; accepted 16 July 2011; published online 29 August 2011)

The titanium tantalum oxide, TiTaO, was fully characterized *in situ* in an integrated metal–insulator–metal (MIM) configuration on a wide frequency band, from 1 mHz to 30 GHz. First, XPS and XRD analysis show that TiTaO dielectric is amorphous and presents Ti-O, Ta-O, and Ti-Ta bounds. Next, by using dedicated MIM test devices and a specific extraction procedure, both relative permittivity κ and loss tangent $\tan\delta$ were extracted on the wide frequency band. The results show a dependence on both frequency and thickness. Conduction mechanism of ion impurities such as oxygen vacancies at very low frequencies (below 0.1 Hz), Maxwell-Wagner relaxations due to space charges at electrode interface (between 0.1 and 5 Hz), and dielectric grain boundaries or hopping (between 1 and 100 MHz) are underlined and studied with temperature measurements. The paper shows the usefulness of *in situ* wideband frequency measurements and that the dielectric permittivity of TiTaO in a 100 nm thick film is decreasing from 86 at 10 kHz to 20 at 10 GHz. © 2011 American Institute of Physics. [doi:10.1063/1.3626067]

I. INTRODUCTION

Recently, a great deal of interest was focused on doped metal oxides like $M^1_x M^2_y O_z$ to improve dielectric properties in comparison with standard compounds. Indeed, electrical characteristics of these materials are promising for many microelectronic applications and it is necessary to investigate their dielectric responses as a function of frequency. The dielectric constant κ can be increased by adding an element with a higher polarizability, like titanium.¹ Current density and leakages J of the structure are decreased by incorporating an element with a higher bandgap, such as silicon or aluminum oxides.^{2,3} The voltage linearity α of the complete stack is also reduced by coupling dielectrics with negative curvature, such as SiO₂ (Ref. 2) or SrTiO₃,⁴ with materials with a positive curvature, such as HfO₂, ZrO₂ (Ref. 5) or HfTiO.⁶ Finally, the choice of materials is motivated by the intended application. For example, in flash memory applications, dielectrics with a relative permittivity between 9 and 30, inclusive, and with a large bandgap, between 3 to 6 eV, are required. In this case aluminum oxide Al₂O₃ is presented as the reference dielectric and so compounds based on aluminates or doped with rare earth are studied.^{7,8} For metal–insulator–metal (MIM) capacitors in DRAM, the scaling of dimensions necessitates finding dielectrics with a relative permittivity between 10 and 50, inclusive, and deposited using an atomic layer deposition (ALD) or atomic vapor deposition (AVD) technique.^{9–11} Several compounds based on hafnium, zirconium, or perovskites with strontium or barium and doped with tantalum, titanium, or niobium are promising.⁸ Solutions for tech-

nologies down to 30 nm have already been demonstrated thanks to bilayer capacitors such as Al₂O₃/HfO₂ or Al₂O₃/ZrO₂.^{12,13} For technologies less than 30 nm, materials based on TiO₂ are excellent candidates, in particular crystalline SrTiO₃ combined with high metal work function electrodes.¹⁴

Several studies have been performed on hafnium, tantalum, aluminum, or zirconium compounds. In Table I, a non-exhaustive list of research works and results obtained for these dielectric combinations are presented. This table draws up an actual state of the art for research. Several studies are still in progress for finding new combinations of dielectrics in order to satisfy the intended application specifications.

In this paper, we will take a special interest in titanium tantalum oxide, Ti_xTa_yO_z. TiO₂, with a very high relative permittivity ranging from 30 to more than 100, depending on the structures (anatase or rutile, respectively), seems to be an excellent candidate for a high- κ dielectric layer in integrated MIM capacitors.²⁸ But, its leakage currents are far too big for the intended applications.²⁹ Conversely, Ta₂O₅ shows a relative permittivity much lower, closer to 25, but also much lower leakage currents.³⁰ By adding TaO into the TiO matrix, the TiO crystallization is blocked and leakage currents are drastically reduced.³¹ However, since TiTaO shows a low bandgap energy, around 3.8 eV (between TiO₂, ~3.3 eV, and Ta₂O₅, ~4.5 eV) according to Ref. 29, metal electrodes with a high metal work function, like iridium (5.2 eV), can be also used, as proposed in Ref. 25. MIM capacitors based on TiTaO have already been developed and demonstrated in Refs. 25 and 26. Thus a 23 fF· μm^{-2} density record has been obtained with a relative permittivity near 39 and a quality factor equal to 120 at 1 GHz (Ref. 28) showing that this material is an interesting high- κ material for designing new integrated devices.

^{a)}Author to whom correspondence should be addressed. Electronic mail: bertaud@ihp-microelectronics.com.

TABLE I. Summary table of electrical performances for high- κ dielectric materials recently investigated.

Compound	Deposition technique	Density C_S [fF · μm^{-2}]	Permittivity κ	Leakages J [nA · cm^{-2}]	Linearity α [ppm · V^{-2}]	Year
AlTiO _x	oxidation	10	15	10^{+9} @ 1 V	2051	2002 (Ref. 15)
AlTaO _x	oxidation	10	18	$3.6 \times 10^{+3}$ @ 1 V	130	2003 (Ref. 16)
Tb 4%-HfO ₂	PVD	13.3	21	$2 \times 10^{+2}$ @ 3.3 V	3000	2003 (Ref. 17)
TaZrO	PVD	12	14	5 @ 1 V	1236	2006 (Ref. 18)
SrTaO	MOCVD	10	20	~ 10 @ 3 V	300	2006 (Ref. 19)
Sr ₂ Ta ₂ O _{7-δ}	AVD	5.5	18.6	7 @ 2 V	80	2008 (Ref. 20)
BiTaO	MOCVD	10	50	~ 10 @ 3 V	600	2006 (Ref. 19)
TiSiO ₄	PVD	8.2	16.5	10 @ 2 V	600	2007 (Ref. 2)
HfAlO _x	PVD	3.5	19	$7.9 \times 10^{+3}$ @ 2.4 V	143	2009 (Ref. 3)
Zr _{1-x} Al _x O ₂	ALD	32.9	33.4	2 @ 1 V	?	2009 (Ref. 21)
HfTiO	IBS/MOCVD	15.5	22.9	$3 \times 10^{+3}$ @ 1 V	3136	2010 (Ref. 4)
ZrTiO ₄	PVD	29.1	49.4	$1.3 \times 10^{+2}$ @ -2 V	2341	2009 (Ref. 22)
HfSiO	Sol-gel	12.1	5	8 @ 5 V	?	2010 (Ref. 23)
ZrSiO	Sol-gel	14.3	8.1	7 @ 5 V	?	2010 (Ref. 23)
Hf _x Zr _{1-x} O	ALD	—	21	—	—	2007 (Ref. 24)
HfZrLaO	ALD	50.7	17.2	$9.3 \times 10^{+8}$ @ 1 V	?	2010 (Ref. 25)
TiTaO	PVD	23	39	$\sim 10^{+4}$ @ 1 V	81	2005 (Ref. 26, 27)

All these dielectrics will be used in applications working at ever higher frequencies, and their behavior depends on this frequency. So, these dielectric materials need to be investigated in a wide frequency band, covering low to microwave frequencies. In this work, the dielectric constant and loss tangent of integrated TiTaO-based MIM devices are investigated as a function of thickness, frequency (from a mHz to a few GHz), and temperature. After the description of the test devices, the physical characterizations of TiTaO thin films will be presented. Then, the wideband frequency characterization procedure will be detailed and applied to this dielectric in order to clarify the dielectric relaxation mechanisms.

II. ELABORATION OF TITAO AND DEDICATED TEST DEVICES

A. Sample realization

TiTaO was deposited by PVD Magnetron of a TiTaO target (composition: Ti_{0.6}Ta_{0.4}O) on a 200 nm thick aluminum bottom electrode. A power of 350 W and a temperature of 350 °C are used as deposition parameters. Three different thicknesses are targeted: 50, 100, and 175 nm, using a growth rate calibrated at 2.8 nm·min⁻¹. The TiTaO layers are first analyzed with a spectroscopic phase modulated ellipsometer UVISEL HORIBA Jobin Yvon. X-ray photoelectron spectroscopy (XPS) are then performed on a customized Thermo Fisher Scientific Theta 300 spectrometer. Finally, x-ray diffraction (XRD) is applied to the layers using a diffractometer, D8 Advanced series II from Bruker. The bottom electrode was etched for designing the bottom dedicated devices and sputtered on a 1 μm thick SiO₂ layer for isolating the high frequency measurements from the silicon substrate. After an ion beam etching (IBE) of the TiTaO dielectric layer with an argon pressure $p_{\text{Ar}} = 1.9 \times 10^{-4}$ mbar and a RF power of $P_{\text{RF}} = 500$ W, a 300 nm aluminum top electrode is deposited by sputtering. The complete stack is described in Fig. 1.

B. Wideband frequency dedicated devices

Dedicated test samples were designed for wideband frequency characterizations, divided into three bands: low, middle, and high frequency ranges. At low frequencies, i.e., from 1 mHz to 1 MHz (called region A), simple one-port parallel MIM capacitors are used, as shown in Fig. 2(a), and measured with a Novocontrol dielectric spectrometer. The ground pad surface is $200 \times 200 \mu\text{m}^2$ and the MIM capacitance surface is $100 \times 100 \mu\text{m}^2$. At middle frequencies, i.e., from 100 kHz to 110 MHz (called region B), one-port parallel MIM capacitors, designed for GSG (ground signal ground) coplanar probe measurements, are used, as shown in Fig. 2(b). These measurements are performed using an Agilent 4294 A Impedance-Meter. The dimensions of the pads are $80 \times 50 \mu\text{m}^2$ for ground pads and $75 \times 75 \mu\text{m}^2$ for the MIM capacitor. At high frequencies, i.e., from 40 MHz to 30 GHz (called region C), four micro-strip waveguides designed with 10 μm or 20 μm widths for the signal line and with 200 μm or 1 mm lengths are used, as shown in Fig. 2(c). Specific high frequency de-embedding devices “Open” and “Thru” are also designed (not shown here). For all these high frequency dedicated devices, an on-wafer Short Open Load Thru (SOLT) calibration is first achieved in order to match the impedance to 50 Ω . The scattering parameters S_{ij} of the complete test structures are then measured using an Anritsu 37397C Vector Network Analyzer (VNA).

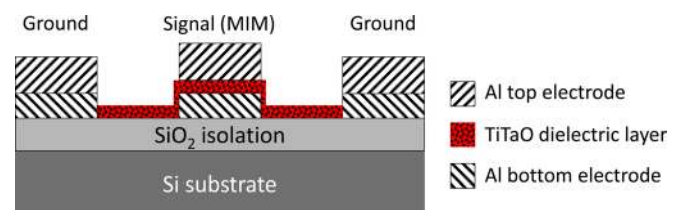


FIG. 1. (Color online) Complete MIM stack integrating TiTaO dielectric layer.

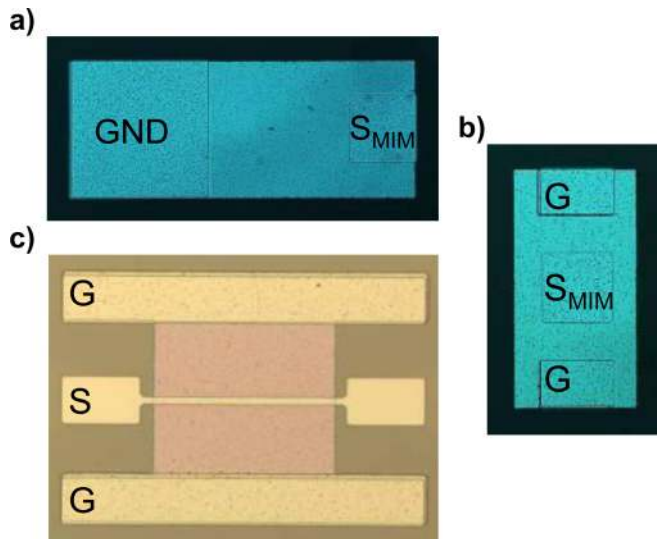


FIG. 2. (Color online) Wideband frequency dedicated MIM devices integrating TiTaO as insulating layer. (a) Simple one-port parallel MIM capacitor for the low frequency measurements. (b) One-port parallel MIM capacitor with GSG contact pads for the middle frequency measurements. (c) A micro-strip line with a length of $L = 200 \mu\text{m}$ and a width of $W = 10 \mu\text{m}$ for the high frequency measurements with the same GSG tips.

By mixing low, middle, and high frequency test devices, ultra wideband frequency characterization (over 14 decades) of these MIM devices can be done to extract the complex permittivity of the inter-metallic insulator. In this paper this procedure is applied to characterize integrated TiTaO as an insulator layer *in situ*.

III. PHYSICAL CHEMISTRY CHARACTERIZATIONS OF THE TITAO

Ellipsometry measurements performed just after deposition exhibit thicknesses of 478, 932, and 1570 Å for a refractive index of 2.3 (at a 632 nm wavelength) and a gap energy of 3.6 eV, according to a Tauc-Lorentz model.³² The ellipsometric results fit quite well to the adjusted thickness during deposition, with the difference increasing with the deposited thickness. The refractive index and material bandgap of TiTaO are between the values for pure TiO_2 ($n_{\text{TiO}_2} = 2.49$ and $E_g^{\text{TiO}_2} \sim 3.3 \text{ eV}$)³³ and pure Ta_2O_5 ($n_{\text{Ta}_2\text{O}_5} = 1.79$ and $E_g^{\text{Ta}_2\text{O}_5} \sim 4.5 \text{ eV}$).³⁴ The optical behavior and material bandgap of our layers are much closer to the TiO_2 values.

An XPS study is performed on the 100 nm TiTaO thick sample to analyze the surface state, in terms of chemical bonding. A high resolution monochromatic Al $K\alpha$ X-ray source (1486.6 eV photons) was used at a pass energy of 60 eV. Carbon 1s, oxygen 1s, tantalum 4f, and titanium 2p core level energy regions are acquired. After the calibration with the carbon 1s peak (due to surface pollution) at 285 eV, a numerical procedure for spectra fitting was performed to extract the peak contributions in the acquired energy regions. Individual line shapes were simulated with a combination of Lorentzian and Gaussian functions. Background subtraction was performed using a Shirley function calculated from a numerical iterative method. First results on the oxygen 1s peaks (not shown here) give three different bounds: a main peak at 532 eV corresponding to the pure element and two sub-peaks

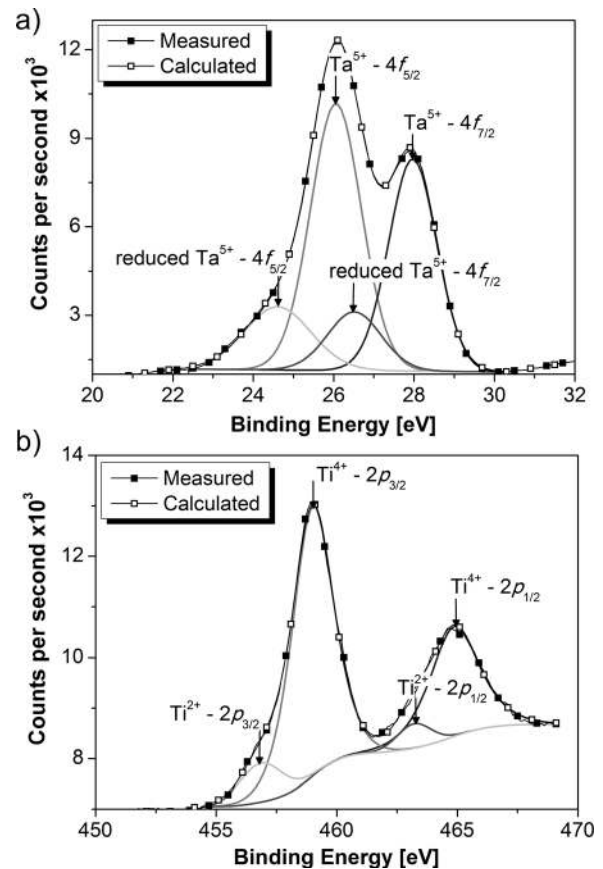


FIG. 3. XPS core level spectra in the Ta 4f (a) and Ti 2p (b) regions. In both parts measured and calculated curves are compared.

for higher and lower binding energies corresponding to oxygen linked to tantalum and titanium, respectively. The peak extraction results for XPS measurements are presented in Fig. 3.

In Fig. 3(a), the different peaks linked to the tantalum 4f core level are observed. Ta^{5+} -O bonds linked to tantalum oxide Ta_2O_5 are clearly visible at 26 and 28 eV. Similarly, in Fig. 3(b), the two peaks at 459 and 465 eV are linked to Ti^{4+} -O bonds of the titanium oxide TiO_2 . Then, in each figure, two sub-peaks are also noticed—close to 24.5 and 26.5 eV in Fig. 3(a), and 457 and 463 eV in Fig. 3(b). These two peaks can be linked to sub-oxidized tantalum, as reduced Ta^{5+} (mixed Ta^{4+} and Ta^{3+} , which are not possible to distinguish in the peak decomposition), and to titanium, as Ti^{2+} . As reported in Ref. 35, the oxygen vacancies replacement in TiTaO dielectric is made with tantalum or titanium, confirming that Ti-Ta bonds can be created and can be at the origin of the reduction of Ta^{5+} and Ti^{4+} . The dielectric layer does not seem to be only a conglomerate of Ta_2O_5 and TiO_2 , a mixed compound is also present.

Then, XRD is performed in a Bragg-Brentano geometry at the Cu $K\alpha 1$ x-ray wavelength, selected using a Ge monochromator. The results for two different areas and stacks including the 175 nm TiTaO layer are shown in Fig. 4. Only peaks related to silicon or aluminum are observed but no signal corresponding to TiTaO could be detected. We can conclude, as obtained in Ref. 36, that TiTaO is amorphous. The

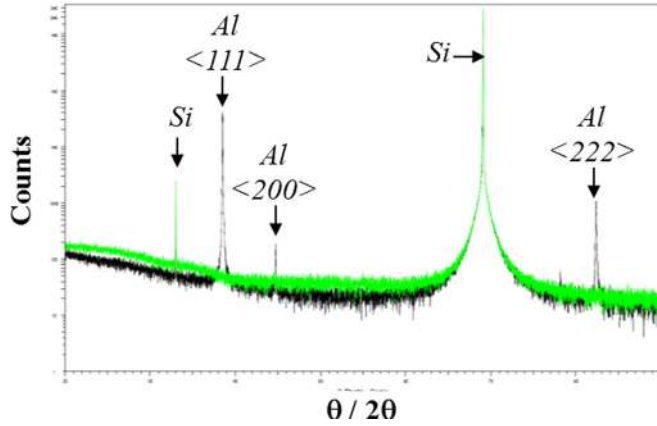


FIG. 4. (Color online) XRD analysis on two different areas. In light color (green online), TiTaO/SiO₂/Si stack is measured, whereas in dark black, TiTaO/Al/SiO₂/Si stack is measured. The different peaks observed are linked to the corresponding element: Al or Si.

same results are obtained for the two other thicknesses, 50 nm and 100 nm.

IV. WIDEBAND FREQUENCY CHARACTERIZATION

Dedicated test devices on wafers, described in Fig. 2, were designed to investigate MIM structures integrating TiTaO dielectric material in a wide frequency band, by mixing low, middle, and high frequency measurements. In the low and middle frequency domains (down to 110 MHz, in regions A and B), one port parallel capacitors present contact pads without access lines, so only parasitic effects of pads are de-embedded using dedicated structures. This section will first present the high frequency characterization procedure before showing results obtained on the TiTaO complex permittivity as a function of the frequency.

A. High frequency measurements procedure

The de-embedding procedure proposed in Ref. 37 is improved to match our system and to extract the impedance of microstrip waveguides, denoted the device under test (DUT), without any parasitic effects due to contact pads and access lines. This technique calculates and removes effects of these two parasitic elements using the electrical equivalent circuit model presented in Fig. 5. In order to apply this de-embedding procedure, two additional dedicated devices (Open and Thru), so called “de-embedding devices,” are needed.

As shown in Fig. 5, the contact pads are modeled by two admittances, G_1 and G_2 . The electrical coupling between contact pads is depicted by G_3 . The impedances Z_1 and Z_2 describe electrical losses and inductive effects of the access

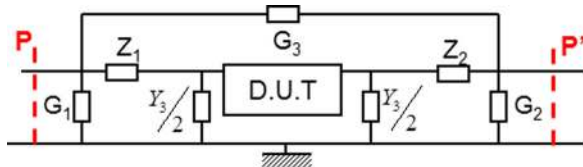


FIG. 5. (Color online) Equivalent electrical model used for the de-embedding procedure to measure intrinsic properties of the DUT.

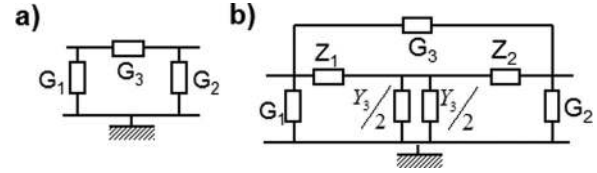


FIG. 6. Equivalent electrical models for Open (a) and Thru (b) de-embedding devices.

lines. The admittance Y_3 represents the capacitive behavior and dielectric losses of these access lines. The measurement planes are located in P and P' after the preliminary Short-Open-Load-Thru calibration of the test set (VNA and prober), which is an automatic and already implemented procedure. These reference planes are then moved to the DUT terminations, behind pads and access lines, when the de-embedding procedure is performed with two dedicated de-embedding devices.

The “Open” de-embedding device is designed with contact pads alone. The “Thru” device is made with the same access lines used to connect contact pads to the DUT. In the first step, the measured S scattering matrix of the “Open” device is converted into the Y admittance matrix, denoted Y_{OPEN} . In accordance with Fig. 5, an equivalent π -model is proposed to describe the behavior of the “Open” device, as shown in Fig. 6(a). So, parasitic elements G_1 , G_2 , and G_3 are calculated from the Y_{OPEN} admittance matrix using Equation (1):

$$\begin{aligned} G_1 &= Y_{11OPEN} - Y_{12OPEN} & G_2 &= Y_{22OPEN} - Y_{21OPEN} \\ G_3 &= -Y_{21OPEN} \end{aligned} \quad (1)$$

In the second step, the measured S scattering matrix of the “Thru” device is converted into the Y admittance matrix. An equivalent electrical model, proposed in Fig. 6(b), allows one to extract Z_1 , Z_2 , and Y_3 . In this step, the contact pad effects are subtracted using the knowledge of G_1 , G_2 , and G_3 .

Finally, the Y-matrix obtained from the scattering matrix measured in P and P' reference planes (Fig. 5) is corrected to give the intrinsic Y-matrix of the DUT, denoted Y_{DUT} , using Equation (2):

$$Y_{DUT} = \left(\left(Y_{PP'} - \begin{bmatrix} G_1 + G_3 & -G_3 \\ -G_3 & G_1 + G_3 \end{bmatrix} \right)^{-1} - \begin{bmatrix} Z_1 & 0 \\ 0 & Z_2 \end{bmatrix} \right)^{-1} - \begin{bmatrix} Y_3/2 & 0 \\ 0 & Y_3/2 \end{bmatrix} \quad (2)$$

So, the parasitic effects of elements G_i , Y_i , and Z_i are totally removed and the two port micro-strip transmission line (DUT) is fully characterized.

After this de-embedding procedure, the micro-strip transmission line is modeled with a complete RLCG (Resistance (R), Inductance (L), Capacitance (C) and Conductance (G)) distributed circuit (by length unit), shown in Fig. 7.

With the values of the capacitance $C_{DUT, 10/20 \mu m}$ and the conductance $G_{DUT, 10/20 \mu m}$ of the two different micro-strip line widths (10 and 20 μm), we are able to extract the relative permittivity κ and loss tangent $\tan\delta$ of the investigated film, in our case the TiTaO dielectric. The difference

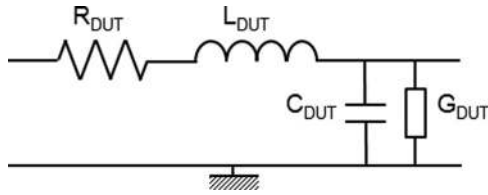


FIG. 7. Equivalent electrical transmission line model of the DUT as an infinitesimal distributed RLCG circuit.

between these extracted capacitances, $C_{DUT,10\mu m}$ and $C_{DUT,20\mu m}$, allows one to remove edge capacitance effects. So, the result gives the capacitance of a line of $10\ \mu m$ width, which can be modeled as a plane capacitance. The permittivity value of TiTaO (κ_{TiTaO}) is extracted from this plane capacitance value with Equation (3) where t_{TiTaO} is the thickness of the film and ϵ_0 the vacuum permittivity. The loss tangent is extracted with the same reasoning, thanks to relation (4) with $G_{DUT,10/20\mu m}$ the conductance of the two different lines and ω the angular frequency.

$$\kappa_{TiTaO} = \frac{(C_{DUT,20\mu m} - C_{DUT,10\mu m})t_{TiTaO}}{\epsilon_0 \times 10 \times 10^{-6}} \quad (3)$$

$$\tan \delta = \frac{G_{DUT,10/20\mu m}}{\omega \times C_{DUT,10/20\mu m}} \quad (4)$$

B. RESULTS AND DISCUSSION

The wideband frequency results, obtained by combining the three different frequency ranges, are presented in this section. First of all, the frequency behavior of the relative permittivity κ for the three different thicknesses, 50, 100, and 175 nm, is given in Fig. 8. The extracted values of the permittivity of TiTaO layers are summarized in Table II for the three thicknesses and three frequency points across the range. First, an excellent agreement is observed between results obtained at the end of low, A (or middle, B), fre-

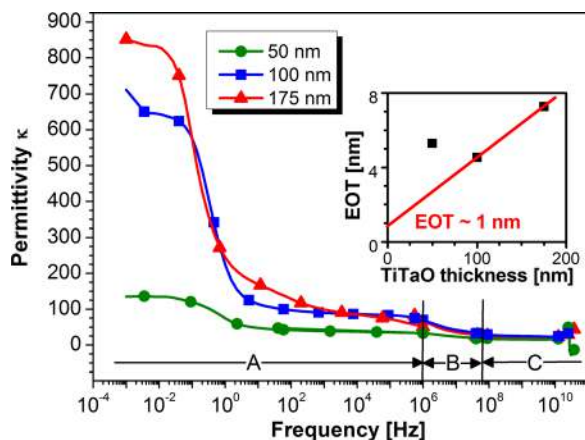


FIG. 8. (Color online) Dependence of the relative permittivity κ with both thickness and frequency. The measurements are done for the three different thicknesses (50, 100, and 175 nm) and from 1 mHz to 30 GHz. Regions A, B, and C correspond to the low frequency (from 1 mHz to 1 MHz), middle frequency (from 100 kHz to 110 MHz), and high frequency (from 40 MHz to 30 GHz) domains, respectively. The inset shows the EOT as a function of the TiTaO thickness t_{TiTaO} , at 10 kHz.

TABLE II. Values of permittivity of TiTaO layers as a function of thickness and frequency.

Frequency/Thickness	50 nm	100 nm	175 nm
10 kHz	37	86	84
10 MHz	23	42	35
10 GHz	13	20	15

quency domain and the beginning of middle, B (or high, C), frequency domain, making our results relevant. Second, a dependence of the permittivity with both thickness and frequency is clearly pointed out. Between 10 kHz and 10 GHz, the permittivity values decrease by 65%, 77%, and 82% for the 50 nm, 100 nm, and 175 nm thick layers, respectively.

The dependence of the permittivity on thickness is discussed in this section. At low frequency, this difference is even more underlined and tends to decrease with increasing frequency, reaching nearly the same value for high frequencies (above 1 GHz). This thickness dependence of the permittivity has already been observed on BaTiO₃, SrTiO₃, and (Ba,Sr)TiO₃ components.^{38–43} Many phenomena can explain the difference of permittivity with thickness: oxygen stoichiometry,³⁹ film composition,⁴⁰ grain size,⁴¹ grain boundaries,⁴² crystallinity,⁴³ strain,³⁸ or interfaces.³⁸ Because our dielectric is amorphous, this thickness dependence cannot be linked to grains or crystallinity. The presence of an interfacial layer, like AlO_x, with a relative permittivity between 5 and 7, can reduce the total permittivity of the layer. By reasoning with the equivalent oxide thickness (EOT), described with Equation (5) where κ_{SiO_2} is the permittivity value of SiO₂, the thickness t_{AlO_x} of the AlO_x interface can be estimated.

$$EOT = \frac{\kappa_{SiO_2}}{\kappa_{TiTaO}} t_{TiTaO} + t_{AlO_x} \quad (5)$$

The deposition process being the same for all samples, the interfacial layer should be identical for all. As shown in the inset of Fig. 8, for the two thick layers, an interfacial layer thickness between 1 and 1.3 nm is calculated by varying with the permittivity value from 5 to 7. But, the thinnest layer does not seem to adopt the same behavior of the two thicker films, proving a difference in the permittivity value. An explanation could be a difference between “bulk-like” properties for the 100 and 175 nm layers and “nanoscale-like” properties for the 50 nm layer. Nevertheless, for this thinnest thickness, the permittivity values are in agreement with Ref. 36, i.e., between 35 and 52, depending on the metal electrodes. The permittivity of TiTaO films seems to be reduced for thicknesses below 100 nm.

Then, for understanding the dependence of the permittivity on the frequency, we plot in Fig. 9 the loss tangent $\tan \delta$ and the relative permittivity κ for the 100 nm thick TiTaO film. As for the permittivity, the measurements of the loss tangent are in agreement for the three different techniques. In dielectric materials, four different polarization mechanisms are possible: electronic, ionic, dipolar, and space charge or interfacial polarization.⁴⁴

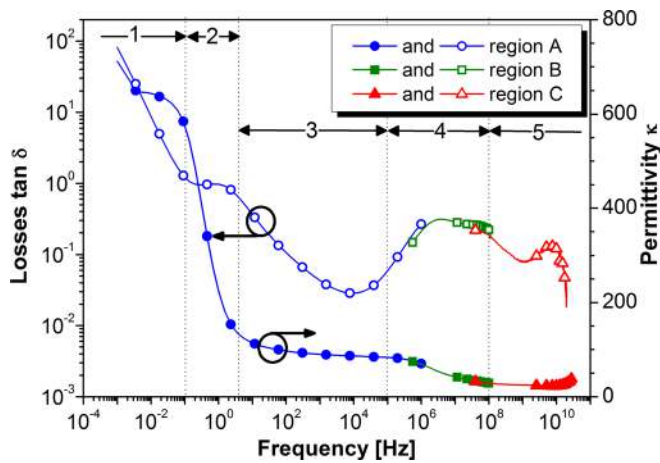


FIG. 9. (Color online) Evolution of the loss tangent $\tan\delta$ (open symbols) and the relative permittivity κ (filled symbols) with frequency for a 100 nm thick TiTaO layer. The blue circles are for region A (low frequency domain), the green squares are for region B (middle frequency domain), and the red triangles are for region C (high frequency domain). The five discussed regions are marked.

We decide to divide these curves into five frequency areas, as indicated in Fig. 9. First, the region up to 0.1 Hz is characterized by a huge constant value of the permittivity, i.e., ~ 650 , and a loss tangent that follows a linear behavior with frequency in a log-log scale. This behavior is linked to the ionic conduction of charged impurities at very low frequency, such as the migration of oxygen vacancies.⁴⁵

Second, the region between 0.1 Hz and 5 Hz is characterized by a strong decrease of the permittivity. This phenomenon is representative of a space charge relaxation at electrode interfaces. Using temperature measurements shown in Fig. 10, a first activation energy E_a^1 of 0.35 eV is found, thanks to the Arrhenius⁴⁶ law of described in Equation (6), where A is a constant describing the relaxation frequency at infinite temperature, $E_a^{(i)}$ is the activation energy of the dielectric relaxation (i), k_B is the Boltzmann constant and T is the temperature in K.

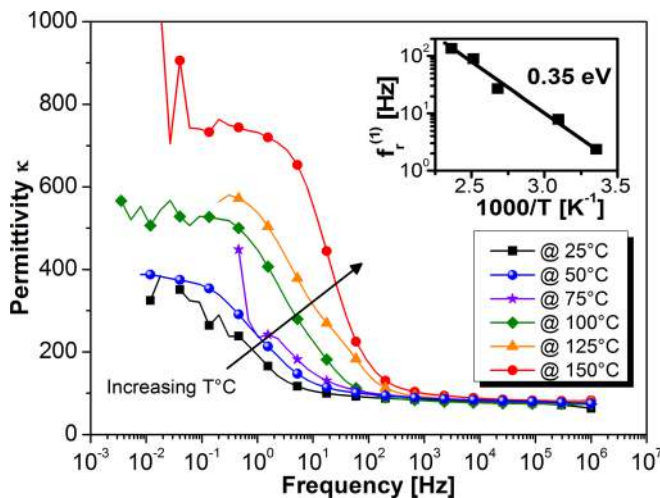


FIG. 10. (Color online) Temperature effect (from room temperature to 150 °C) in the low frequency domain (from 10 mHz to 1 MHz) on the permittivity of a 100 nm thick TiTaO layer. The inset shows the dependence of the relaxation frequency f_r^1 on temperature.

$$f_r^{(i)} = A \exp\left(-E_a^{(i)}/k_B T\right) \quad (6)$$

This behavior in very low frequency domains is well described by Coelho modeling,⁴⁷ referred to a Maxwell-Wagner relaxation due to surface charges pileup at the electrodes-dielectric boundaries. The value obtained is in the same order of the one obtained by Kim *et al.*,⁴⁸ 0.90 eV for SrBi₂Ta₂O₉, and by Lee *et al.*,⁴⁴ 0.72 eV for BaTiO₃. The relaxation is linked here to the charge carrier of oxygen vacancy impurities, considered as the most mobile intrinsic ionic defect. Baiatu *et al.*⁴⁹ also suggested that the oxygen vacancy plays an important role in the dielectric degradation of (Ba,Sr)TiO₃ films.

The third region, between 10 Hz and 100 kHz, shows the well-known values of permittivity and losses, i.e., near 90 and 0.03, respectively, at 10 kHz. Besides, the temperature capacitance coefficient (TCC, α_T), which characterizes the capacitance linearity according to the temperature, is calculated at 10 kHz and a value of 2711 ppm·°C⁻¹ is found. This value is above the 558 ppm·°C⁻¹ obtained in Ref. 27, but there a 17 nm thick layer was investigated.

The fourth region, between 1 MHz and 100 MHz, shows that a second dielectric relaxation occurs, characterized by an increase (a “bump”) in the losses and a decrease of the permittivity, to be discussed in detail below. Finally, in the fifth region, above 1 GHz, the high frequency behavior of the dielectric layer is observed and the values of permittivity or loss tangent are respectively 22 and 0.08 at 10 GHz.

The second dielectric relaxation, which occurs near 10 MHz in the frequency area 4, is now discussed in detail. In this frequency domain, this relaxation could be explained by a dipolar relaxation or a Debye-like relaxation due to space charge interfacials not located at the electrode interfaces but at the grain boundaries,⁵⁰ or hopping. Hopping is a polarization due to the ionic motion of defects by jumping from one site to another.⁵¹ We will consider now these three hypotheses for explaining the relaxation. First, our material is amorphous; this relaxation cannot be dipolar and linked to dipoles. Second, it is known that the Maxwell-Wagner relaxation occurs in heterogeneous systems in which the dielectric components have different conductivities. Liu *et al.*⁵⁰ report that the grains and grain boundaries are responsible for the relaxation arising at their interfaces in this frequency range near 1 MHz. For explaining this behavior, the temperature dependence of the permittivity and the loss tangent have been characterized in middle (results not shown) and high frequency domains, as presented in Fig. 11.

In the high frequency domain, the temperature has a strong influence on the dielectric properties. A TCC α_T value of 1490 ppm·°C⁻¹ is found at 1 GHz, which is lower than the one in the low frequency domain, and can be linked to the Voltage Capacitance Coefficient α (VCC) which decreases with increasing frequency.⁵² In Fig. 11(b), the increase of the loss tangent with temperature is typical for a semi-conductor material, as proved by the Steinhart-Hart equation,⁵³ and linked to the decrease of resistivity with the rising temperature [(refer to Equation (4)]. For explaining the dielectric relaxation at 10 MHz, the Arrhenius law of

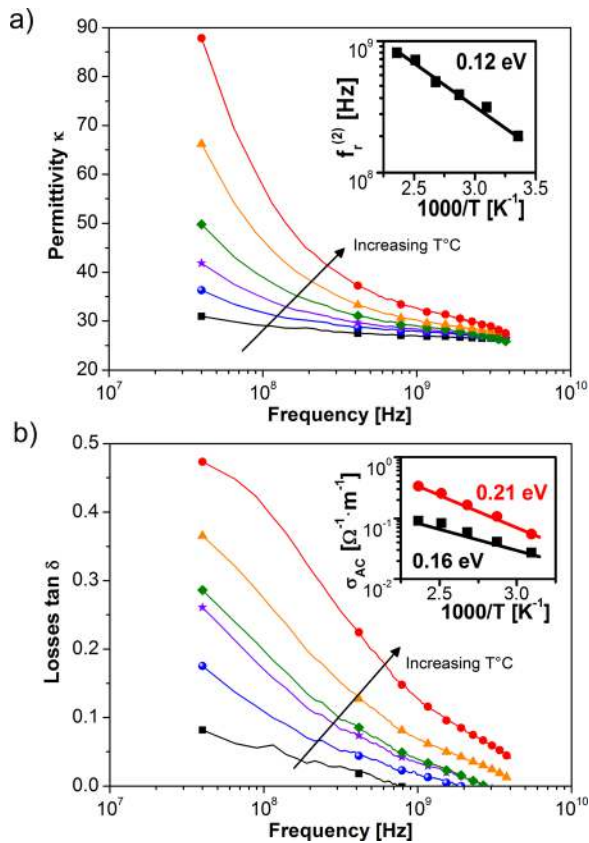


FIG. 11. (Color online) Temperature effect in the high frequency domain (from 40 MHz to 4 GHz) on the permittivity (a) and the loss tangent (b) of a 175 nm thick TiTaO layer. The inset in (a) shows the dependence of the relaxation frequency $f_r^{(2)}$ on temperature. The inset in (b) shows the dependence of the ac conduction σ_{AC} on temperature for two frequencies: 40 MHz (in black squares) and 414 MHz (in red circles). The symbols used indicate the same temperatures as used in Fig. 10.

Equation (6) is applied as before and an activation energy E_a^2 of 0.12 eV is extracted, as shown in the inset of Fig. 11(a). A first conclusion is that this second relaxation is less impressed than the one at very low frequency, according to these values. This second dielectric relaxation cannot be linked only to space charge relaxation at the dielectric grain boundaries. Thirdly, as mentioned in Ref. 51, the contribution of hopping is described with the calculation of the thermal activation of the ac conduction, according to Equation (7), where B is a constant and E_{cond} is the activation energy for conduction.

$$\sigma_{AC} = B \exp(-E_{cond}/k_B T) \quad (7)$$

The values of the ac conductivity σ_{AC} are obtained thanks to the extracted values of the conductance G and can be linked to the loss tangent. In the inset of Fig. 11(b), the activation energies of 0.16 and 0.21 eV are obtained at 40 MHz and 414 MHz. These values are close to the values in Ref. 51: 0.17 eV and also close to the activation energy value for a Maxwell-Wagner relaxation. Lee *et al.*⁴⁴ suggested that if the relaxation mechanism is governed by hopping, the value of E_a^2 is expected to be close to, or less than, that of E_{cond} . To prove a Debye-like relaxation and the presence of TiO_x or TaO_x nano-domains responsible for this relaxation at their

boundaries, Cross-Sectional Transmission Electron Microscopy (XTEM) studies are necessary to complete this analysis. At this stage, it is not possible to validate one model for this second relaxation: Debye-like at grain boundaries, or hopping? In order to avoid such a decrease in permittivity values, optimization techniques have to be found for keeping the high permittivity values between the low and high frequency ranges. Post-annealing processes have to be explored to develop such high- κ materials for RF or DRAM applications. It also has been reported that an oxygen plasma treatment significantly improves the electrical characteristics by passivating the oxygen vacancies.⁵⁴

V. CONCLUSION

TiTaO-based MIM structures have been characterized in an ultra-wideband frequency, from 1 mHz to 30 GHz, thanks to dedicated test devices for high frequency measurements. XRD and XPS analysis show that our dielectric is amorphous, with Ti-O, Ta-O, and Ti-Ta bounds, proving that the system is not only a conglomerate of Ta₂O₅ and TiO₂. Electrical and frequency studies demonstrate that the TiTaO permittivity is dependent on both thickness and frequency. This shows the requirements to evaluate the permittivity and more generally the dielectric behavior in the high frequency domain for future applications in RF devices. Two relaxations in the TiTaO were evaluated. The first one (closed to 1 Hz) is related to space charges, such as oxygen vacancies at the electrode interface and with an activation energy of 0.35 eV. The second one (close to 10 MHz) can be related to a hopping phenomenon or a Maxwell-Wagner relaxation, which occurs at the grain boundaries of our material. This relaxation leads to a strong diminution of the permittivity values between the kHz and GHz ranges, from near 90 to 22. Finally, this wideband frequency methodology can be applied to several other dielectrics in order to study the dielectric properties in the high frequency range for the optimization of future RF applications.

ACKNOWLEDGMENTS

The authors would like to acknowledge the “Rhône-Alpes” region and the cluster “Micro-Nano,” via the “Mini-II” project, for supporting this research, and MHS Industry Nantes for TiTaO deposition. This work has also been realized with the help of the “Plateforme Technologique Amont” of Grenoble. The authors would also like to thank Hervé Roussel, from LMGP, for XRD measurements and Serge Blonkowski, from STMicroelectronics Crolles, for fruitful discussions.

¹D. Brassard, D. K. Sarkar, M. A. El Khakania, and L. Ouellet, *J. Vac. Sci. Technol. A*, **24**(3), 600, 2006.

²D. Brassard, L. Ouellet, and M. A. El Khakani, *IEEE Electron Device Lett.*, **28**(4), 261, 2007.

³M.K. Hota, C. Mahata, S. Mallik, B. Majhi, T. Das, C.K. Sarkar, and C. K. Maiti, in Proceedings of the 2nd International Workshop on Electron Devices and Semiconductor Technology, Bombay, 1–2 June 2009. Available at http://ieeexplore.ieee.org/xpls/abs_all.jsp?arnumber=5166109.

⁴C. Jorel, C. Vallée, P. Gonon, E. Gourvest, C. Dubarry, and E. Defay, *Appl. Phys. Lett.*, **94**, 253502, 2009.

- ⁵T. Bertaud, C. Bermond, T. Lacrevez, C. Vallée, Y. Morand, B. Fléchet, A. Farcy, M. Gros-Jean, and S. Blonkowski, *Microelectron. Eng.*, **87**, 301, 2010.
- ⁶B.-Y. Tsui, H.-H. Hsu, and C.-H. Cheng, *IEEE Electron Device Lett.*, **31**(8), 875, 2010.
- ⁷S. Govindarajan, T.S. Boscke, P. Sivasubramani, P. D. Kirsch, B. H. Lee, H.-H. Tseng, R. Jammy, U. Schroder, S. Ramanathan, and B. E. Gnade, *Appl. Phys. Lett.*, **91**, 062906, 2007.
- ⁸J. A. Kittl, K. Opsomer, M. Popovici, N. Menou, B. Kaczer, X. P. Wang, C. Adelman, M. A. Pawlak, K. Tomida, A. Rothschild, B. Govoreanu, R. Degraeve, M. Schaeckers, M. Zahid, A. Delabie, J. Meersschant, W. Polspoel, S. Clima, G. Pourtois, W. Knaepen, C. Detavernier, V. V. Afanas'ev, T. Blomberg, D. Pierreux, J. Swerts, P. Fischer, J. W. Maes, D. Manger, W. Vandervorst, T. Conard, A. Franquet, P. Favia, H. Bender, B. Brijs, S. Van Elshocht, M. Jurczak, J. Van Houdt, and D. J. Wouters, *Microelectron. Eng.*, **86**, 1789, 2009.
- ⁹M. Schumacher, P. K. Baumann, and T. Seidel, *Chem. Vap. Deposition*, **12**, 99, 2006.
- ¹⁰X. Garros, C. Leroux, D. Blin, J.-F. Damlencourt, A.-M. Papon, and G. Reimbold, in *Proceedings of the 32nd European Solid-State Device Research Conference*, pp. 411–414, Firenze, 24–26 September 2002. Available at http://ieeexplore.ieee.org/xpls/abs_all.jsp?arnumber=1503885.
- ¹¹C. Wenger, M. Lukosius, I. Costina, R. Sorge, J. Dabrowski, H.-J. Müssig, S. Pasko, and C. Lohe, *Microelectron. Eng.*, **85**, 1762, 2008.
- ¹²K. Kim and G. Jeong, *Tech. Dig. - Int. Electron. Devices Meet.*, **27**, 2007. Available at http://ieeexplore.ieee.org/xpls/abs_all.jsp?arnumber=4418854.
- ¹³T. Schloesser, F. Jakubowski, J. V. Kluge, A. Graham, S. Slesazek, M. Popp, P. Baars, K. Muemmler, P. Moll, K. Wilson, A. Buerke, D. Koehler, J. Radecker, E. Erben, U. Zimmermann, T. Vorrath, B. Fischer, G. Aichmayr, R. Agaiby, W. Pamler, T. Schuster, W. Bergner, and W. Mueller, *Tech. Dig. - Int. Electron. Devices Meet.*, 809, 2008.
- ¹⁴S. W. Lee, J. H. Han, and C. S. Hwang, *Electrochem. Solid-State Lett.*, **12**(11), G69, 2009.
- ¹⁵S. B. Chen, C. H. Lai, A. Chin, J. C. Hsieh, and J. Liu, *IEEE Electron Device Lett.*, **23**(4), 185, 2002.
- ¹⁶M. Y. Yang, C. H. Huang, A. Chin, C. Zhu, M. F. Li, and D.-L. Kwong, *IEEE Electron Device Lett.*, **24**(5), 306, 2003.
- ¹⁷S. J. Kim, B. J. Cho, M.-F. Li, C. Zhu, A. Chin, and D.-L. Kwong, *IEEE Electron Device Lett.*, **24**(7), 442, 2003.
- ¹⁸N. Inoue, H. Ohtake, L. Kume, N. Furutake, T. Onodera, S. Saito, A. Tanabe, M. Tagami, M. Tada, and M. Hayashi, in *Proceedings of the International Interconnect Technology Conference*, pp. 63–65, San Francisco, 5–7 June 2006.
- ¹⁹L. Goux, H. Vander Meeren, and D. J. Wouters, *J. Electrochem. Soc.*, **153**(7), F132, 2006.
- ²⁰M. Lukosius, C. Wenger, S. Pasko, I. Costina, J. Dabrowski, R. Sorge, H.-J. Müssig, and C. Lohe, *IEEE Electron Device Lett.*, **55**(8), 2273, 2008.
- ²¹W. Weinreich, R. Reiche, M. Lemberger, G. Jegert, J. Müller, L. Wilde, S. Teichert, J. Heitmann, E. Erben, L. Oberbeck, U. Schröder, A.J. Bauer, and H. Ryssel, **86**, 1826, 2009. Available at <http://www.sciencedirect.com/science/article/pii/S0167931709002421>.
- ²²Y.-H. Wu, B.-Y. Chen, L.-L. Chen, J.-R. Wu, and M.-L. Wu, *Appl. Phys. Lett.*, **95**, 113502, 2009.
- ²³J. S. Meena, M.-C. Chu, and F.-H. Ko, in *Proceedings of the 3rd International NanoElectronics Conference*, Hong Kong, 3–8 January 2010.
- ²⁴R. I. Hegde, D. H. Triyoso, S. B. Samavedam, and B. E. White, Jr., *J. Appl. Phys.*, **101**, 074113, 2007.
- ²⁵C. H. Liu and H.W. Chen, *Microelectron. Reliab.*, **50**, 599, 2010.
- ²⁶K. C. Chiang, C. C. Huang, A. Chin, W. J. Chen, S. P. McAlister, H. F. Chiu, J.-R. Chen, and C. C. Chi, *IEEE Electron Device Lett.*, **26**(7), 504, 2005.
- ²⁷K. C. Chiang, C. H. Lai, A. Chin, T. J. Wang, H. F. Chiu, J.-R. Chen, S. P. McAlister, and C. C. Chi, *IEEE Electron Device Lett.*, **26**(10), pp. 728, October 2005.
- ²⁸S. K. Kim, W.-D. Kim, K.-M. Kim, C. S. Hwang, and J. Jeong, *Appl. Phys. Lett.*, **85**(18), 4112, 2004.
- ²⁹K. C. Chiang, C. H. Lai, A. Chin, H. L. Kao, S. P. McAlister, and C. C. Chi, in *Proceedings of the IEEE Microwave Theory and Technique (Symp. Dig.)*, Long Beach, 12–17 June 2005.
- ³⁰M. Thomas, A. Farcy, C. Perrot, E. Deloffre, M. Gros-Jean, D. Benoit, C. Richard, P. Caubet, S. Guillaumet, R. Pantel, M. Cordeau, J. Piquet, C. Bermond, B. Fléchet, B. Chenevier, and J. Torres, in *Proceedings of VLSI Technology Symposium*, pp. 58–59, 12–14 June 2007.
- ³¹K. C. Chiang, Albert Chin, C. H. Lai, W. J. Chen, C. F. Cheng, B. F. Hung, and C. C. Liao, in *Proceedings of VLSI Technology Symposium*, pp. 62–63, Kyoto, 14–16 June 2005.
- ³²G. E. Jellison, Jr. and F. A. Modine, *Appl. Phys. Lett.*, **69**(3), 371, 1996.
- ³³H. Tang, K. Prasad, R. Sanjinès, P. E. Schmid, and F. Lévy, *J. Appl. Phys.*, **75**(4), 2042, 1994.
- ³⁴F. Rubio, J.M. Albella, J. Denis and J.M. Martinez-Duart, *J. Vac. Sci. Technol.*, **21**(4), 1043, 1992.
- ³⁵E. Atanassova, D. Spassov, A. Paskaleva, M. Georgieva, and J. Koprinarova, *Thin Solid Films*, **516**, 8684, 2008.
- ³⁶M. Lukosius, C. B. Kaynak, C. Wenger, G. Ruhl, and S. Rushworth, *J. Vac. Sci. Technol. B*, **29**(1), 2011.
- ³⁷E. P. Vandamme, D. M. M. P. Schreurs, and G. Van Dinther, *IEEE Trans. Electron Devices*, **48**(4), 737, 2001.
- ³⁸S. K. Streiffer, C. Basceri, C. B. Parker, S. E. Lash, and A. I. Kingon, *J. Appl. Phys.*, **86**(8), 4565, 1999.
- ³⁹W. J. Lee, I.-K. Park, G.-E. Jang, and H.G. Kim, *Jpn. J. Appl. Phys.*, **34**(1), 196, 1995.
- ⁴⁰K. Abe and S. Komatsu, *J. Appl. Phys.*, **77**(12), 6461, 1995.
- ⁴¹C. S. Hwang, S. O. Park, H.-J. Cho, C. S. Kang, H. K. Kang, S. I. Lee, and M. Y. Lee, *Appl. Phys. Lett.*, **67**(19), 2819, 1995.
- ⁴²K. Abe and S. Komatsu, *Jpn. J. Appl. Phys.*, **33**(9B), 5297, 1994.
- ⁴³T. Kuroiwa, Y. Tsunemine, T. Horikawa, T. Makita, J. Tanimura, N. Mikami, and K. Sato, *Jpn. J. Appl. Phys.*, **33**(9B), 5187, 1994.
- ⁴⁴S.-J. Lee, K.-Y. Kang, and S.-K. Han, *Appl. Phys. Lett.*, **75**(12), 1784, 1999.
- ⁴⁵F. El Kamel, P. Gonon, and C. Vallée, *Appl. Phys. Lett.*, **91**, 172909, 2007.
- ⁴⁶A.K. Jonscher, *J. Phys. D: Appl. Phys.*, **32**(14), R57, 1999.
- ⁴⁷R. Coelho, in *IEEE Conference on Electrical Insulation and Dielectric Phenomena*, Minneapolis, 19–22 October 1997.
- ⁴⁸I. W. Kim, C. W. Ahn, J. S. Kim, T. K. Song, J.-S. Bae, B. C. Choi, J.-H. Jeong, and J.S. Lee, *Appl. Phys. Lett.*, **80**(21), 4006, 2002.
- ⁴⁹T. Baiatu, R. Waser, and K.-H. Härdtl, *J. Am. Ceram. Soc.*, **73**(6), 1663, 1990.
- ⁵⁰J. Liu, C.-G. Duan, W. N. Mei, R. W. Smith, and J. R. Hardy, *J. Appl. Phys.*, **98**, 093703, 2005.
- ⁵¹J. Wang, X. G. Tang, H. L. W. Chan, and C. L. Choy, *Appl. Phys. Lett.*, **86**, 152907, 2005.
- ⁵²T. Bertaud, S. Blonkowski, C. Bermond, C. Vallée, P. Gonon, M. Gros-, and B. Fléchet, *IEEE Electron Device Lett.*, **31**(2), 114, 2010.
- ⁵³J. S. Steinhart and S. R. Hart, *Deep-Sea Res. Oceanogr. Abstr.*, **15**(4), 497, 1968.
- ⁵⁴D.-C. Shye, C.-C. Hwang, M.-J. Lai, C.-C. Jaing, J.-S. Chen, S. Huang, M.-H. Juang, B.-S. Chiou, and H.-C. Cheng, *Jpn. J. Appl. Phys.*, **42**(2A), 549, 2003.